

Displacement Analysis of Solar Magnetic Field Images in EUV Wavelengths of Space Solar Telescope

Yang Liu^{*,†,‡}, Kefei Song^{*,§}, Xiaodong Wang^{*,¶}, Bo Chen^{*,||},
Junlin Ma^{***} and Zhenwei Han^{*,††}

**Changchun Institute of Optics, Fine Mechanics and Physics
Chinese Academy of Sciences, Changchun 130033, P. R. China*

*†University of Chinese Academy of Sciences
Beijing 100049, P. R. China*

‡liuy_ciom@163.com

§songkefei@sina.com

¶wangxd@ciomp.ac.cn

||chenb@ciomp.ac.cn

****michael8446@126.com*

††hanzhenwei1234@163.com

Received 28 May 2018

Accepted 25 July 2018

Published 19 September 2018

In this paper, the combination of nonlinear gradient iteration and crossing method is presented in order to analyze high precision remote sensing images of solar magnetic field in extreme ultra-violet (EUV) wavelengths which are usually affected by solar magnetic evolution, satellite attitude changes and random satellite jitter, and to reduce structural complexity the complicated correlation tracker is normally adopted. Using crossing method which better approached the inefficiency by computing full-scale solar magnetic field images, nine point areas are uniformly selected in full-scale solar magnetic field images which solves the problem of low-computing efficiency. Meanwhile, nonlinear gradient iteration algorithm through numerical simulation experiments is adopted to analyze displacement of solar magnetic field images in EUV wavelengths, which reduces the errors due to the solar intensity changing and tiny deformation of solar magnetic field compared to traditional algorithms. The results clearly indicate that the precision of mean error field and square deviation field for deformed displacement are both less than 5% of pixel by solar magnetic field images of Solar Dynamics Observatory (SDO).

Keywords: Solar magnetic field images; displacement analysis; EUV; nonlinear gradient iteration; mean error; parabolic least-square fit algorithm.

1. Introduction

The research of solar physics on sensor requirements of high-spatial resolution of solar magnetic field images has already reached to the order of magnitude of arcsec

^{‡,§,¶} Corresponding authors.

and sub-arcsec. Therefore, the requirements for observation instruments are becoming more demanding. For space solar telescope, although there is no atmospheric interference, the orbital precession and the attitude changes of spacecraft^{1,6} and the revolving of the moving parts all will cause the random vibration of the platform of the spacecraft^{9,17,18} which will cause image blurring that will affect the high imaging precision of space solar telescope. Therefore, taking measures to suppress vibration of the platform of spacecraft or realizing solar magnetic field images registration in EUV wavelengths to obtain solar magnetic image with high-spatial resolution, high-precision displacement analysis^{2,7} is very necessary.

Since compared to adaptive optical systems, image stabilizers are more simpler and less expensive, using image stabilizers is especially rewarding. Due to the solar images in EUV, wavelengths are very blurred and without obvious characteristics, and also the local features of the solar are changing with the changing of the solar itself (with time-varying shapes, exhibits extended, irregular), some detecting technologies for measuring the displacement of solar magnetic field using centroid and limb measurements are unfit. Therefore, compensation technique based on motion blur which uses statistical properties between images, which is correlation tracker technology,^{4,5,13} greatly satisfies the demand of analyzing the displacement of spacecraft by images.

$$C_{R,L}(\Delta x, \Delta y) = \sum_{x=0}^{M-1} \sum_{y=0}^{N-1} R(x, y) \cdot L(x + \Delta x, y + \Delta y), \quad (1)$$

where $C_{R,L}$ denotes a two-dimensional spatial coordinate between the reference image $R(x, y)$ and live images $L(x, y)$.

The Chinese Space Solar Telescope (SST) takes $240 \mu s$ for 32- by-32 points complex FFT with increasing hardware complexity and parallel algorithm and achieves an accuracy of about 0.3-pixel with 25-point parabolic least-square fit.

In 1993, the correlation tracker integrated successfully in the system of IAC (Instituto de Astrofísica de Canarias), in 2006, Solar Optical Telescope Onboard (SOLAR-B) researched associatively and developed by Japan and the US also carried this system.¹⁴ The Solar Optical Telescope onboard SOLAR-B achieved 0.09 arcsec sub-pixel size within 20 Hz bandwidth. When the correlation tracker (CT) system starts to work, reference image is considered as the first image grabbed. Live images, which are also called successive images, are used to compare with the reference image in real time. Then analyze spatial lags $\Delta x, \Delta y$ of the two associative images by a relationship of the spatial cross-correlation function. The crest value of the cross-correlation function is the two pictures matching greatly. The relative displacement between reference images and live images is shown in the maximum position. Use parabolic least-square fit algorithm to analyze displacements which possess the sub-pixel accuracy where the two orthogonal x and y directions with the sub-field around the maximum, usually adopting quadratic polynomial fitting

function, which can be written as

$$R(x_i, y_j) = b_1 y_j^2 + b_2 x_i^2 + b_3 y_j x_i + b_4 y_j + b_5 x_i + b_6, \quad (2)$$

where (x_i, y_j) are the integral coordinate values around the maximum position, and $R(x_i, y_j)$ are the corresponding correlation coefficients, and $b_1, b_2, b_3, b_4, b_5, b_6$ are the undetermined coefficients.

SOLAR-B researched together and developed by Japan and the US, the vacuum tower telescopes belonging to the National Solar Observatory at Sacramento, project ANGARA on the Big Solar Vacuum Telescope^{2006,16} all calculate the displacement using solar granulation^{3,15} where solar images are visible wavelength (629–634 nm) obtained by the camera as shown in Fig. 1 obtained from Solar Optical Telescope (SOLAR-B SOT), the bright granulations are not changed over time and distributed, the sunspots are some dark areas on the solar heliosphere surface, where the background temperature slowly drops from 6,000 degrees Celsius to 4,000 degrees Celsius, where the region appears as a dark spot on the surface of the solar.

The spatial solar imager uses the solar EUV images to detect the image displacement caused by the satellite itself and the evolution of the solar in real time. Advantages of calculating the displacement using solar granulation images in visible wavelength (629–634 nm) are that optical systems in visible wavelength are easy to design, including detectors and optical lenses. Solar granulation changes slowly compared to solar magnetic field images in EUV wavelength for solar activities, so it is relatively easy to use solar granulation images in visible wavelength (629–634 nm) to calculate the displacement. Shortcomings of calculating the displacement using solar granulation images in visible wavelength (629–634 nm) are structural complexity for which complicated correlation tracker is normally adopted. Compared to adaptive optical systems that image stabilizers are more simpler and less expensive, so using image stabilizers is especially rewarding.

For solar activities such as solar prominence, solar flares, solar corona and sunspots^{8,19} are mainly shown in short-wave EUV and X-ray bands. It is more accuracy to know solar active rhythm which can increase the accuracy of weather forecast by observing the solar by space solar imager in this wave band. Solar magnetic field

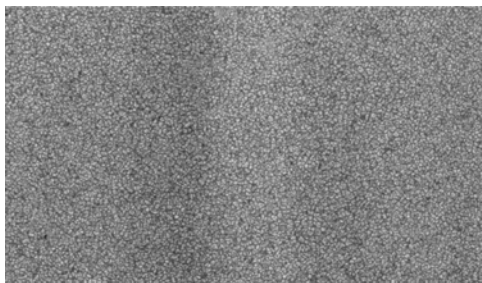


Fig. 1. Image of solar granulations in visible wavelength (629–634 nm).

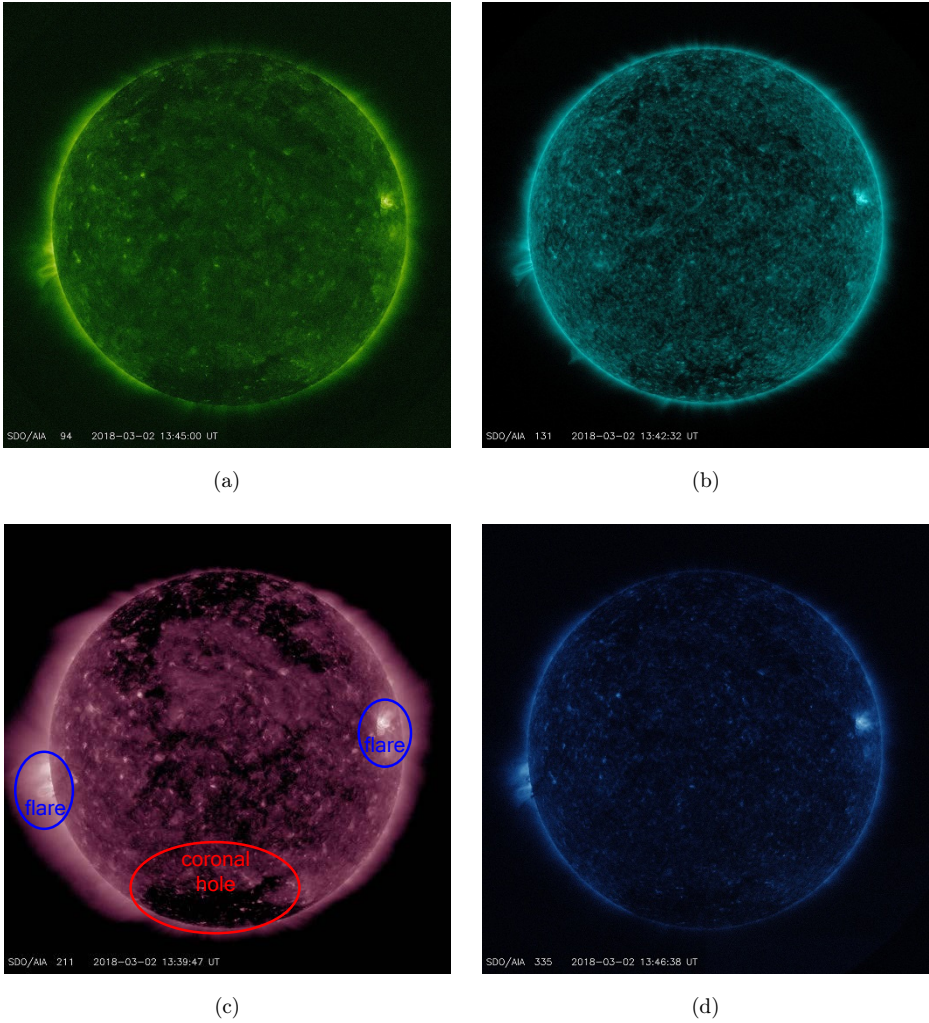


Fig. 2. Solar magnetic field images in EUV wavelength: (a) in wavelength 94 Å, (b) in wavelength 131 Å, (c) in wavelength 211 Å and (d) in wavelength 335 Å.

images of space solar telescope in EUV wavelength obtained from SDO AIA (Atmospheric Imaging Assembly) which takes series remote sensing images of the solar atmosphere through multi-band are shown in Fig. 2, which is 8-bit with dimensions of 4096×4096 pixels in RGB, then we convert the truecolor image RGB to the grayscale intensity image by forming a weighted sum of the R, G, and B components with $0.2989R + 0.5870G + 0.1140B$, in order to link the transformation from the surface area to interior variation, and these four images taken within 6 min could be supposed to be taken at the same time, that the consistency of the algorithm to extreme ultraviolet image processing could be verified. The corona is the

outermost layer of the solar’s atmosphere, radiating energy outwards through X-rays or ultraviolet short wavelengths, you can see large, irregular dark areas in the corona, which is called a coronal hole, and the distribution of the coronal hole can reach most of the solar’s surface, especially in the polar regions of the solar. Solar flares are a kind of intense solar activity, and in the speckle near the active area, a sudden increase of light is seen in small areas. In a matter of minutes, they can be brightened several times or even dozens of times, and mainly occur in short-wave radiation (X-ray and ultraviolet), and their lifespan is between minutes and dozens of minutes, and the brightness rises quickly and falls slowly. The flares appear frequently and the intensity is stronger, especially in the solar peak year. The earth ionosphere is sensitive to changes in solar soft X-ray radiation. Therefore, the X-ray flares are graded based on the soft X-ray radiation intensity of 1–8 angstrom widely used in the world. At present, the flares are divided into five levels, namely, A, B, C, M and X, respectively, as the energy released increased in sequence, according to the magnitude of the peak flow of soft X-rays observed by the GOES satellite. The continuous solar EUV images collected by the space solar imager are directly collimated with high precision on the ground to enhance the signal-to-noise ratio of the images, and higher resolution images could be obtained, there is no need to provide image displacement through indirect detection of the visible wavelength (629–634 nm) image, and the application of this method is not highly time-sensitive.

Figure 3 shows the histogram drawings of solar granulation images in visible wavelength in picture (a) and the four solar magnetic field images in EUV wavelength in picture (b). Picture (a) in Fig. 3 shows that histogram of the solar granulation images in visible wavelength has approximately normal distribution. It also shows that the gray level is concentrated in the higher gray level, the left sides and right sides are roughly symmetrical. However, from picture (b) to picture (e) we can see that there is no obvious rule in histograms of solar magnetic field images in EUV wavelength, and the distribution is in a lower grayscale range and is more discrete.

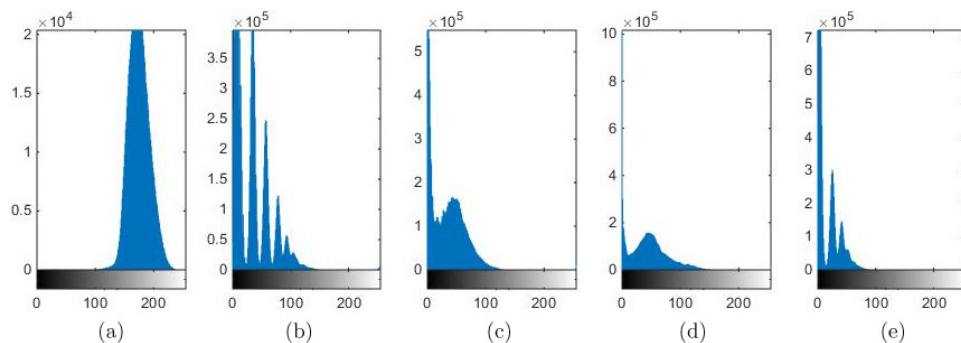


Fig. 3. Histograms of visible wavelength images and EUV wavelength images of solar magnetic field: (a) in visible wavelength (629–634 nm), (b) in wavelength 94 Å, (c) in wavelength 131 Å, (d) in wavelength 211 Å and (e) in wavelength 335 Å.

Among these pictures, we can see that the histogram of solar magnetic field images in 94 Å wavelength and the histogram of solar magnetic field images in 335 Å wavelength are quite similar, which both present the multi-peak discrete distribution. Meanwhile, the histograms of solar magnetic field images in 131 Å wavelength and the histogram of solar magnetic field images in 211 Å wavelength are very similar, which both present single peak continuous distribution. These two grayscale distributions of the histograms of solar magnetic field images in EUV wavelength would cause displacement analysis of solar magnetic field images in EUV wavelengths merging two similar distributions, it will be discussed and verified in what follows.

2. Displacement Analysis Algorithm of Solar Magnetic Field Images by Nonlinear Gradient Iteration

2.1. Model of intensity variation

We can find that previous papers assumed that the elementary hypothesis of the algorithm is that the gray value at a physical point is approximately invariant between a random point of the reference part area and the homologous point of the changed part area, and the equation of this method can be expressed as²⁰

$$\beta(x_j, y_j) = \varphi(x'_j, y'_j), \quad j = 1, 2, \dots, m, \quad (3)$$

where $\beta(x_j, y_j)$ is the gray intensity value at the point (x_j, y_j) of the reference subset image, $\varphi(x'_j, y'_j)$ is the gray intensity at the homologous point (x'_j, y'_j) of the deformed part region, m is the quantity of pixels contained in the reference subset. However, in the deformed images at different time the solar magnetic field evolution and the rapid change in the solar active area usually exists and the offset and gain variation of imaging device and nonuniform sensor pixels as well. Consequently, in order to minimize measurement error, a more practical intensity variation model could be adopted. Therefore, the connection of the intensity value of a physical point between the reference part region and the homologous point in the deformed part region can be expressed by a nonlinear intensity variation model,¹⁰ which considering the scope and offset value of intensity is shown in Fig. 4.

$$a \times \beta^3(x_j, y_j) + b \times \beta(x_j, y_j) + c = \varphi(x'_j, y'_j) \quad (4)$$

where b and a are the linear and cubic factors of the intensity changes, respectively, and c presents the offset of the intensity changes.

2.2. Nonlinear gradient iterative algorithm

The solar magnetic field is continuously varying, so the solar image is deformed. In order to analyze the deformed displacement values of a point (x_c, y_c) , we need to select a square subset around it. If the subset is small enough, the deformation gradient of the subset in the changed image is invariable, and the coordinates of the points (x'_j, y'_j) of the changed part region mapped to the points (x_j, y_j) around the

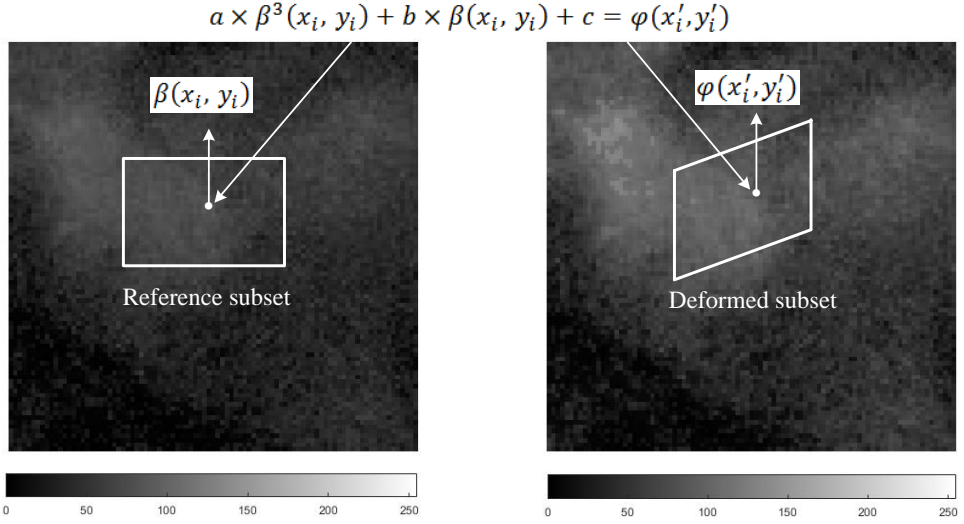


Fig. 4. Intensity variation model of solar magnetic field images in EUV wavelengths with the point in the reference part 91×91 pixels and deformed part 91×91 pixels.

part center (x_c, y_c) in the subset of reference could be indicated as

$$x'_j = x_j + \Delta\sigma + \sigma_x \Delta x_j + \sigma_y \Delta y_j, \quad (5)$$

$$y'_j = y_j + \Delta\tau + \tau_x \Delta x_j + \tau_y \Delta y_j, \quad (6)$$

where $\Delta\sigma$ and $\Delta\tau$ are the sub-pixel shift parameters of the reference part center in orthorhombic directions, respectively; Δx_j and Δy_j are the difference values from (x_j, y_j) to the subset center (x_c, y_c) , $\Delta x_j = x_j - x_c$, $\Delta y_j = y_j - y_c$. Substituting Eqs. (5) and (6) into Eq. (4), the expression of the intensity at the point (x'_j, y'_j) in the deformed part region and its homologous point (x_j, y_j) of the part of reference image could be shown as:

$$Q_j(\mathbf{P}) = \varphi(x'_j, y'_j) - a \times \beta^3(x_j, y_j) - b \times \beta(x_j, y_j) - c \cong 0, \quad (7)$$

where $\mathbf{P} = [\Delta\sigma, \sigma_x, \sigma_y, \Delta\tau, \tau_x, \tau_y, a, b, c]^T$ is the requested argument vector that includes sub-pixel displacement gradients and displacements of the part, Eq. (7) $\mathbf{Q}(\mathbf{P})$ can be solved by iteration algorithm as¹²

$$\mathbf{Q}(\mathbf{P}^{k+1}) = \mathbf{Q}(\mathbf{P}^k) + \nabla \mathbf{Q}(\mathbf{P}^k)(\mathbf{P}^{k+1} - \mathbf{P}^k) = 0, \quad (8)$$

where \mathbf{P}^k and \mathbf{P}^{k+1} are the solutions in the iterative process, respectively.

$$\nabla Q_j(\mathbf{P}) = [\varphi_{x_j}, \varphi_{x_j} \Delta x_j, \varphi_{x_j} \Delta y_j, \varphi_{y_j}, \varphi_{y_j} \Delta x_j, \varphi_{y_j} \Delta y_j, -\beta_j^3, -\beta_j, -1], \quad (9)$$

where φ_{x_j} and φ_{y_j} are the orthorhombic directional spatial gradient values of the deformed subset of the point (x'_j, y'_j) , respectively.

For the $j = 1, 2, \dots, m (m > 9)$ points, the solution of Eq. (8) can be acquired by the iterative least squares method as

$$\mathbf{P}^{k+1} = \mathbf{P}^k - [\nabla\mathbf{Q}(\mathbf{P}^k)^T \nabla\mathbf{Q}(\mathbf{P}^k)]^{-1} \nabla\mathbf{Q}(\mathbf{P}^k)^T \nabla\mathbf{Q}(\mathbf{P}^k). \quad (10)$$

It should be considered that starting value of the unknown vector \mathbf{P} must be given before an iterative procedure. $\mathbf{P} = [\Delta\sigma, \sigma_x, \sigma_y, \Delta\tau, \tau_x, \tau_y, a, b, c]^T$ is the requested argument vector, and $\sigma_x, \sigma_y, \tau_x, \tau_y$, which are sub-pixel displacement gradients, are actually much less than $\Delta\sigma, \Delta\tau$, which are the sub-pixel shift parameters of the reference part center in orthorhombic directions, respectively, so the initial values of $\sigma_x, \sigma_y, \tau_x, \tau_y$ are generally set to zero, b and a are the linear and cubic factors of the intensity changes, respectively, and c presents the offset of the intensity changes. In a short-exposure time, solar magnetic field evolution is mostly linear, so the initial values of a, c are generally set to zero, the linear b factor of the intensity changes converge around 1 according to multiple simulation verification. $\Delta\sigma$ and $\Delta\tau$ are the sub-pixel shift parameters of the reference part center in orthorhombic directions, respectively. According to the experimental results, when the initial values of p and q are selected as 0.2 and 0.1, respectively, the number of iterations is the lowest. In this paper, the initial value \mathbf{P} of iteration can be adopted as $\mathbf{P}^0 = [0.2, 0, 0, 0.1, 0, 0, 0, 1, 0]^T$. The convergence condition of the iterative procedure is repeated until the calculation tolerance $\|\Delta\mathbf{P}^k\|_2 \leq 0.01$ or reaching the maximum number of iterations.

The gray level $\varphi(x'_j, y'_j)$ and its corresponding gradients $\varphi_{xj}, \varphi_{yj}$ must be provided, because the iterative points may not be at internal-pixel position during iterative process. The general interpolation algorithm is cubic spline and bilinear interpolation. The bilinear interpolation is to calculate the grayscale value based on the grayscale value of the four adjacent points around it. The influence of the direct adjacent points has been taken into account. The cubic spline interpolation considers the influence of direct adjacent points, but also takes into account the influence of 16 surrounding adjacent points. Because the solar activity in a short period of time is not particularly severe, there will be no high frequency change, and there is need to deal with the high frequency signal, bilinear interpolation is much less than cubic interpolation, and bilinear linear interpolation can satisfy accuracy requirement, therefore, this paper uses the bilinear interpolation. After gray $\varphi(x'_j, y'_j)$ is calculated by adopting the bilinear interpolation algorithm, we get 41-by-41 matrix of gray $\varphi(x'_j, y'_j)$, however, Barron operator needs to calculate $\varphi(x_j^{(k)} - 2, y_j^{(k)}), \varphi(x_j^{(k)} - 1, y_j^{(k)}), \varphi(x_j^{(k)} + 1, y_j^{(k)}), \varphi(x_j^{(k)} + 2, y_j^{(k)}), \varphi(x_j^{(k)}, y_j^{(k)} - 2), \varphi(x_j^{(k)}, y_j^{(k)} - 1), \varphi(x_j^{(k)}, y_j^{(k)} + 1), \varphi(x_j^{(k)}, y_j^{(k)} + 2)$, so the 41-by-41 matrix of gray $\varphi(x'_j, y'_j)$ is extended to a 45-by-45 matrix, and the newly added data refer to the data of the former 41-by-41 matrix of gray $\varphi(x'_j, y'_j)$ closest to the original data. In this way, 41-by-41 matrix of the gradients $\varphi_{xj}, \varphi_{yj}$ can be implemented with

Barron operator¹¹

$$\begin{aligned} \varphi_x(x_j^{(k)}, y_j^{(k)}) &= \frac{1}{12} \varphi(x_j^{(k)} - 2, y_j^{(k)}) - \frac{8}{12} \varphi(x_j^{(k)} - 1, y_j^{(k)}) \\ &\quad + \frac{8}{12} \varphi(x_j^{(k)} + 1, y_j^{(k)}) - \frac{1}{12} \varphi(x_j^{(k)} + 2, y_j^{(k)}), \end{aligned} \quad (11)$$

$$\begin{aligned} \varphi_y(x_j^{(k)}, y_j^{(k)}) &= \frac{1}{12} \varphi(x_j^{(k)}, y_j^{(k)} - 2) - \frac{8}{12} \varphi(x_j^{(k)}, y_j^{(k)} - 1) \\ &\quad + \frac{8}{12} \varphi(x_j^{(k)}, y_j^{(k)} + 1) - \frac{1}{12} \varphi(x_j^{(k)}, y_j^{(k)} + 2), \end{aligned} \quad (12)$$

$$\begin{aligned} \varphi(x_j^{(k+1)}, y_j^{(k+1)}) &= (1 - \sigma_j)(1 - \tau_j) \varphi(x_j^{(k)}, y_j^{(k)}) + \sigma_j(1 - \tau_j) \varphi(x_j^{(k)} + 1, y_j^{(k)}) \\ &\quad + \tau_j(1 - \sigma_j) \varphi(x_j^{(k)}, y_j^{(k)} + 1) + \sigma_j \tau_j \varphi(x_j^{(k)} + 1, y_j^{(k)} + 1), \end{aligned} \quad (13)$$

where $\sigma_j = \Delta\sigma + \sigma_x \Delta x_j + \sigma_y \Delta y_j$, $\tau_j = \Delta\tau + \tau_x \Delta x_j + \tau_y \Delta y_j$.

3. Checking the Deformed Displacement Field Images Measurement in EUV Wavelengths by Numerical Simulated Experiments

3.1. Image processing to imitate the solar magnetic images evolution in EUV wavelengths

In order to analyze the capacity of the presented algorithm for modified displacement measurement of the solar magnetic field images, numerical simulated experiments are conducted in this article owing to their easily controlled features.

First, reference images are downloaded from SDO, which are 8-bit solar EUV magnetic field images with dimensions of 4096×4096 pixels as shown in Fig. 2, then bilinear interpolation scheme is used ranging from 0.1 to 0.9 pixels by a pace of 0.1 pixels in both y direction and x direction to generate a series of translated images. After that the shifted images are adjusted further artificially with brightness increased by 10%. For solar activities^{18,19} such as solar prominence, solar flares, solar corona and sunspots mainly show in short-wave EUV and X-ray bands, we should consider that the deformed images at different time usually exist in the solar magnetic field evolution and the rapid change in the solar active area and the offset and gain variation of imaging device and nonuniform sensor pixels as well. Afterwards, images are handled to imitate true solar magnetic activation in EUV waveband using the following mapping function:

$$Q_{\text{out}} = \begin{cases} 1.2 \times Q_{\text{in}}, & \text{if } Q_{\text{in}} \geq 0.9 Q_{\text{in_max}}, \\ 1.1 \times Q_{\text{in}}, & \text{if } 0.8 Q_{\text{in_max}} \leq Q_{\text{in}} < 0.9 Q_{\text{in_max}}, \\ Q_{\text{in}}, & \text{if } Q_{\text{in}} < 0.08 Q_{\text{in_max}}, \end{cases} \quad (14)$$

where Q_{out} and Q_{in} are on behalf of the solar field images which are after and before handling, and $Q_{\text{in_max}}$ is the maximum gray value of each image.

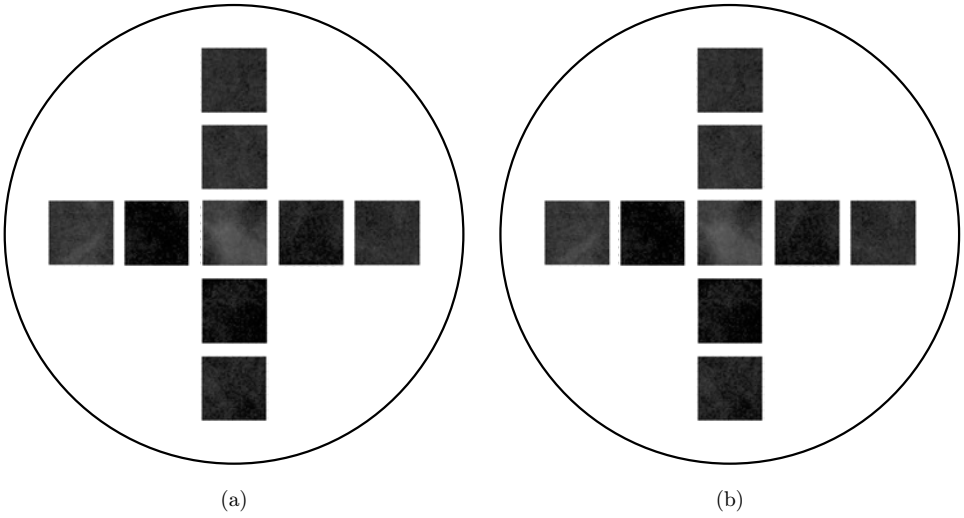


Fig. 5. Crossing method schematic figure of subsets selection method in 211 Å wavelength, and translation value in x direction as same as y direction is 0.9 pixels, and 30% increase in brightness: (a) nine reference subsets, (b) nine corresponding deformed subsets.

In theory, you can take four points in the orthogonal direction to calculate the deformed displacements of the translated images of the solar magnetic field images, but because solar activities such as solar prominence, solar flares, solar corona and sunspots are randomly distributed on the surface of the solar. In order to improve the precision, the algorithm mentioned in this paper is adopted, using crossing scheme at homogeneously distributed 9 points, the deformed displacements of the translated images of the solar magnetic field images are calculated. On the Solar Optical Telescope onboard SOLAR-B jointly developed by Japan and the United States,¹⁴ the displacement is achieved with the 13 shifted pixel areas.

Using crossing scheme at homogeneously distributed 9 points (see Fig. 5, the distance between neighboring points is $1/3$ solar image radius with a subset size of 41×41 pixels.), the deformed displacements of the translated images of the solar magnetic field images are calculated.

3.2. Verification of parabolic least-square fit algorithm for deformed displacement field images measurement in EUV wavelengths

Using parabolic least-square fit algorithm described in Sec. 1 and image processing method described in Sec. 3.1, the mean error and square deviation of the displacement of solar magnetic field images can be analyzed. In Fig. 6, note that the results from 94 Å resemble those from 131 Å and 335 Å, in the y direction, as sub-pixel displacement increases, there are small fluctuations about the mean error and square deviation, and the error is small. However, in the x direction, as sub-pixel

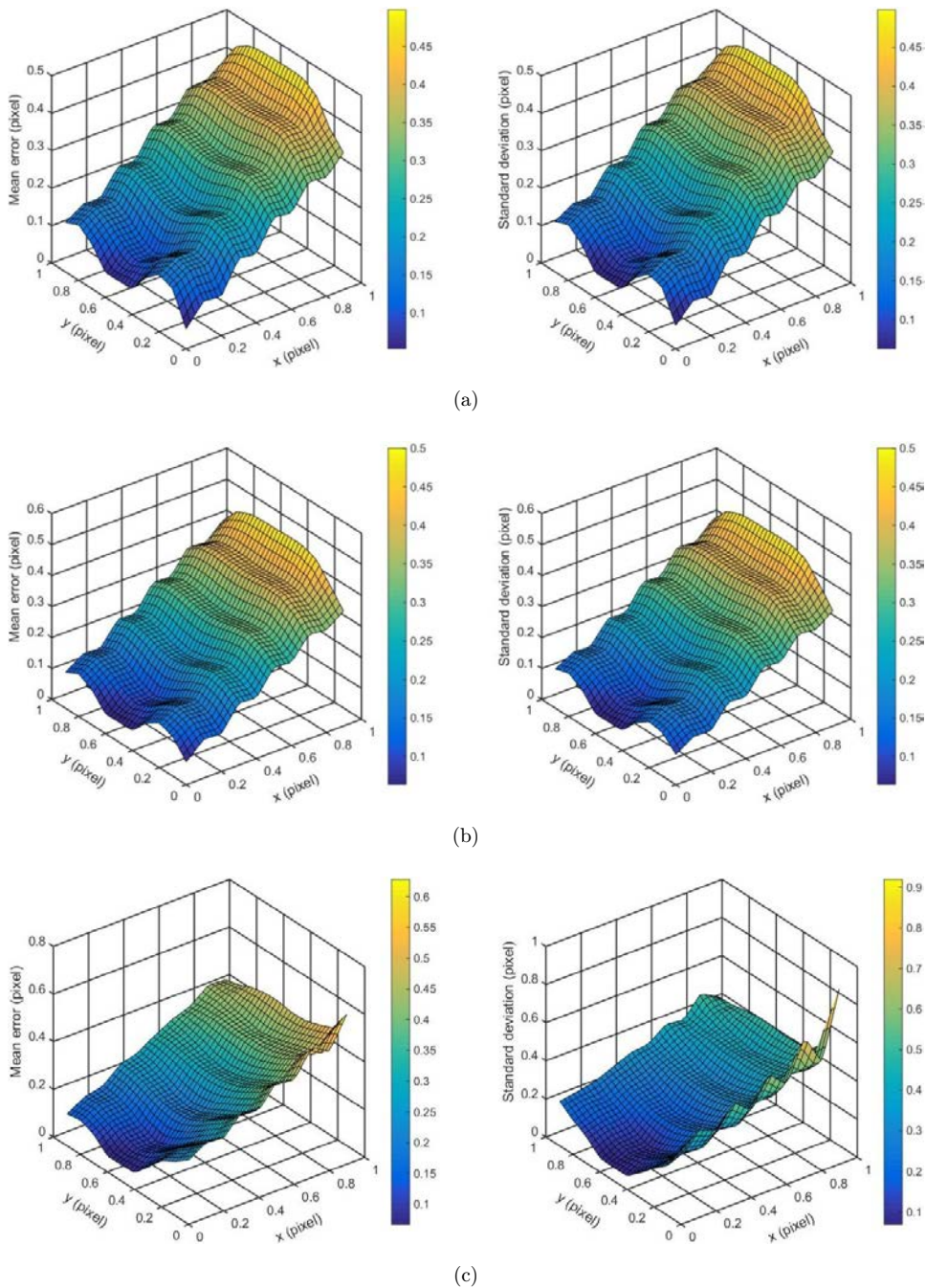


Fig. 6. Curves of mean error field and square deviation field of the displacement of solar magnetic field images in EUV wavelengths by parabolic least-square fit algorithm, and 10% increase in brightness: (a) in wavelength 94 Å, (b) in wavelength 131 Å, (c) in wavelength 211 Å and (d) in wavelength 335 Å.

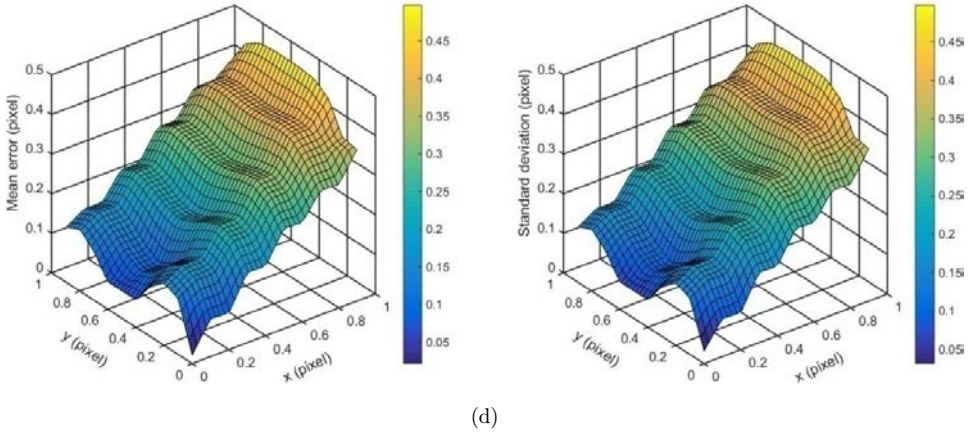
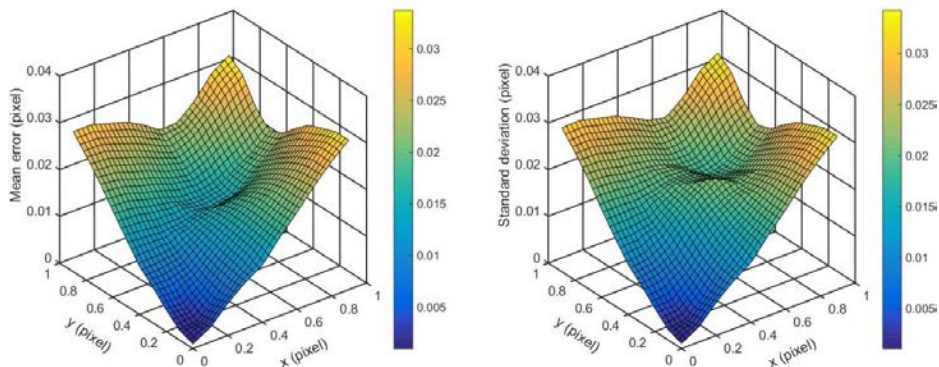


Fig. 6. (Continued)

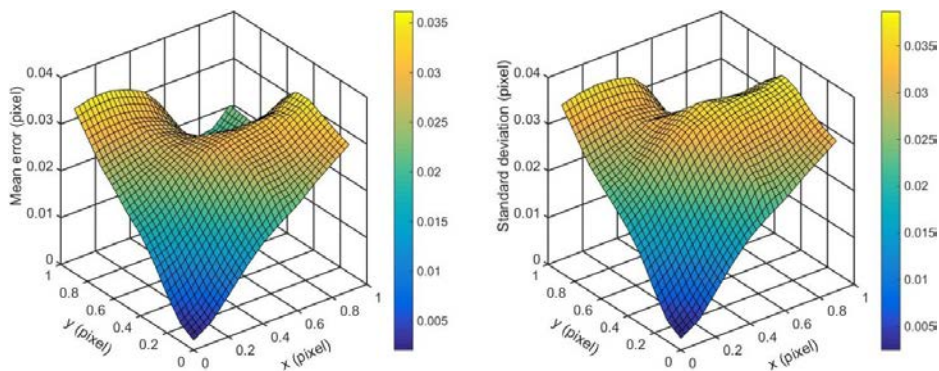
displacement increases, there are small fluctuations about the mean error and square deviation, but the error is much bigger. At the same time, for the mean error and square deviation of the displacement of solar magnetic field images calculated by 221 \AA , which is similar to the other three bands, only the calculation results in 0 sub-pixel y direction are much bigger than the results in the other three bands. It can be known that using this method the mean error and square deviation of the displacement of solar magnetic field images are both less than 50% in all EUV wavelengths, which are much bigger compared to the calculation results using nonlinear gradient iterative algorithm calculated in Sec. 3.3. The primary reason is that the parabolic least-square fit algorithm considering the gray value at a physical point is invariant between a random point of the reference part area and the homologous point of the changed part area as expressed in Eq. (3), and also that the deformed images at different time usually exist in the solar magnetic field evolution and the rapid change in the solar active area and the offset and gain variation of imaging device and nonuniform sensor pixels as well.

3.3. Verification of nonlinear gradient iterative algorithm for deformed displacement field images measurement in EUV wavelengths

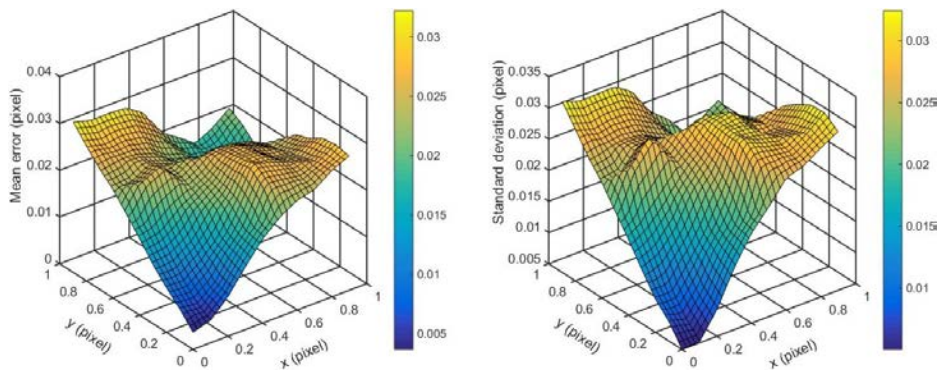
Using nonlinear gradient iterative algorithm described in Sec. 2.2 and image processing method described in Sec. 3.1, the mean error and square deviation of the displacement of solar magnetic field images in EUV wavelengths can be accurately analyzed. In Fig. 7, note that the results from 94 \AA resemble those from 335 \AA owing to their similar histogram distribution, and the mean error and square deviation are minimum near 0 sub-pixel in x direction displacement and 0 sub-pixel y direction displacement, moreover the maximum values of the mean error and square deviation are near three positions: near 0 sub-pixel in x direction displacement and 0.9 sub-pixel y direction displacement, near 0.9 sub-pixel in x direction displacement



(a)



(b)



(c)

Fig. 7. Curves of mean error field and square deviation field of the displacement of solar magnetic field images in EUV wavelengths by nonlinear gradient iterative algorithm, and 10% increase in brightness: (a) in wavelength 94 Å, (b) in wavelength 131 Å, (c) in wavelength 211 Å and (d) in wavelength 335 Å.

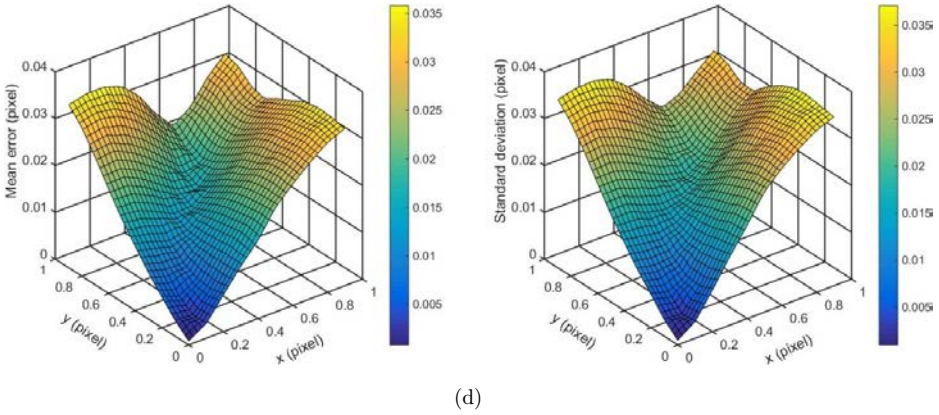


Fig. 7. (Continued)

and 0 sub-pixel y direction displacement, and near 0.9 sub-pixel in x direction displacement and 0.9 sub-pixel y direction displacement. At the same time, the mean error and square deviation of the displacement of solar magnetic field images calculated by 221 Å and 131 Å are almost similar due to their semblable histogram distribution, the minimum position is the same as 94 Å and 335 Å, however, the maximum values of the mean error and square deviation are an area from 0.9 sub-pixel in x direction displacement and 0 sub-pixel y direction displacement to 0 sub-pixel in x direction displacement and 0.9 sub-pixel y direction displacement, it can be known that using this method the mean error and square deviation of the displacement of solar magnetic field images are both less than 5% in all EUV wavelengths, the calculation results are much smaller than the calculation results which use parabolic least-square fit algorithm calculated in Sec. 3.2, the primary reason is that nonlinear gradient iterative algorithm considering the connection of the intensity value of a physical point between the reference part region and the homologous point in the deformed part region can be expressed by a nonlinear intensity variation model as expressed by Eq. (4), and the solar magnetic field evolution and satellite attitude changes during solar magnetic field images acquisition can be easily incorporated, too.

3.4. Verification of the algorithm sensitivity to the solar magnetic evolution and computational efficiency by nonlinear gradient iterative algorithm

Applying the numerical simulated intensity variation scheme, two intensity variation cases (in which brightness are augmented by 20% and 30%) for each translated image are achieved, as it is described in Sec. 3.1. Using the identical measurement scheme in Sec. 2.2, the deformed displacements of the solar magnetic field images in EUV wavelengths are analyzed. The mean error and square deviation of the

calculated deformed displacements under the applied sub-pixel displacements which have various intensity alteration cases is illustrated in Figs. 8 and 9, and the results show clearly that the mean error and square deviation computed increased in brightness by 20% and 30% compared to those in Fig. 7, which are almost the analogical distribution. Furthermore, similar behavior is shown in different intensity variation cases, suggesting that for the solar magnetic field evolution, the method in this paper has well accuracy and stability.

3.5. Verification of integration times of deformed displacement field images measurement in EUV wavelengths by nonlinear gradient iterative algorithm

A comparison of integration times of deformed displacement field images measurement in EUV wavelengths by nonlinear gradient iterative algorithm as ranged

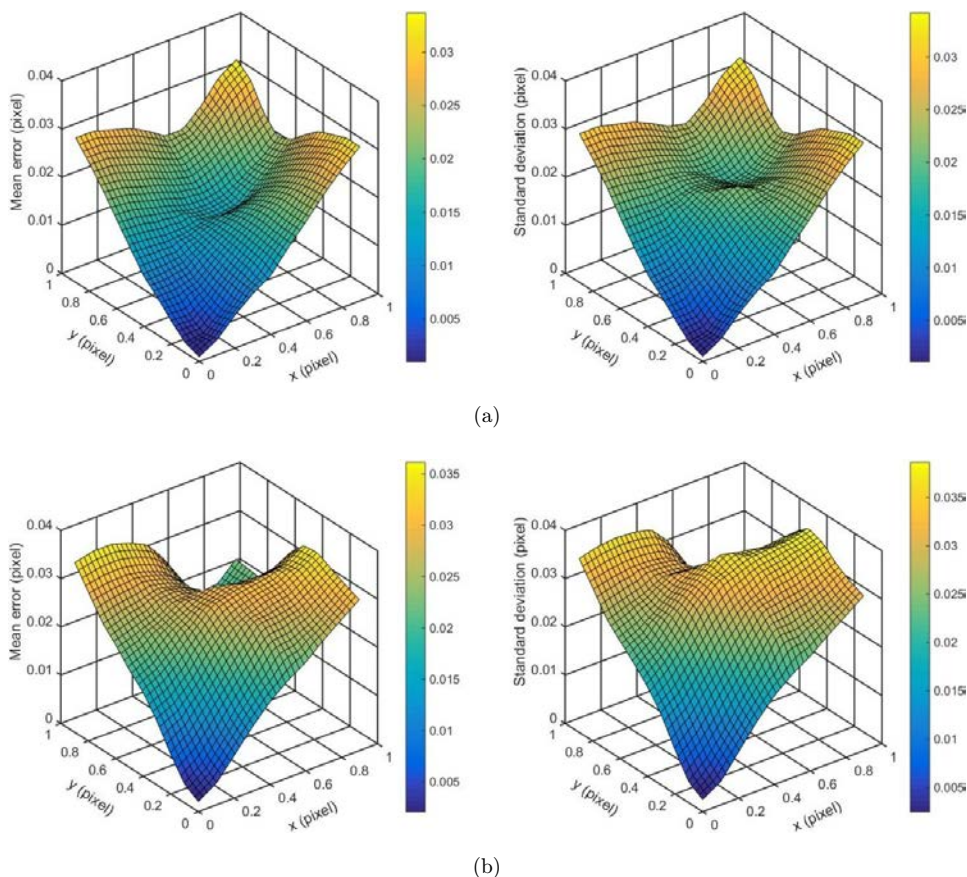
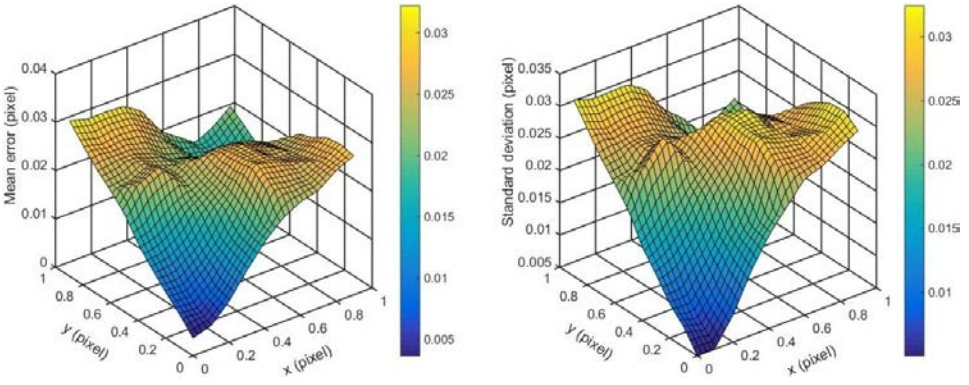
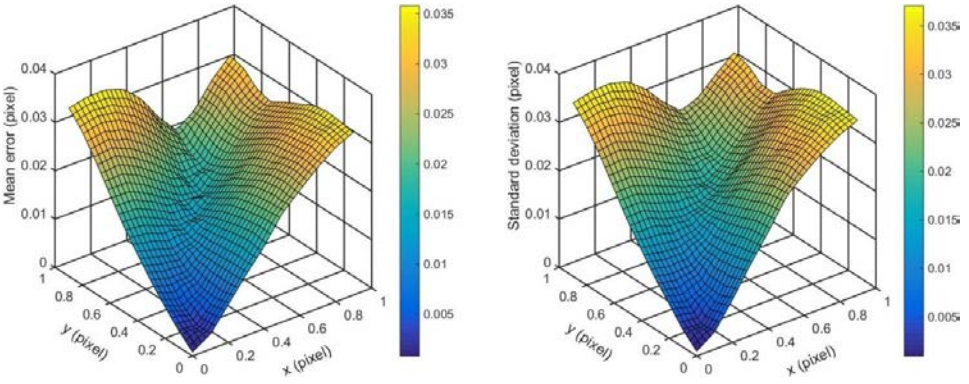


Fig. 8. Graphs of mean error field and square deviation field of the displacement of solar magnetic field images in EUV wavelengths by nonlinear gradient iterative algorithm, and 20% increase in brightness: (a) in wavelength 94 Å, (b) in wavelength 131 Å, (c) in wavelength 211 Å and (d) in wavelength 335 Å.

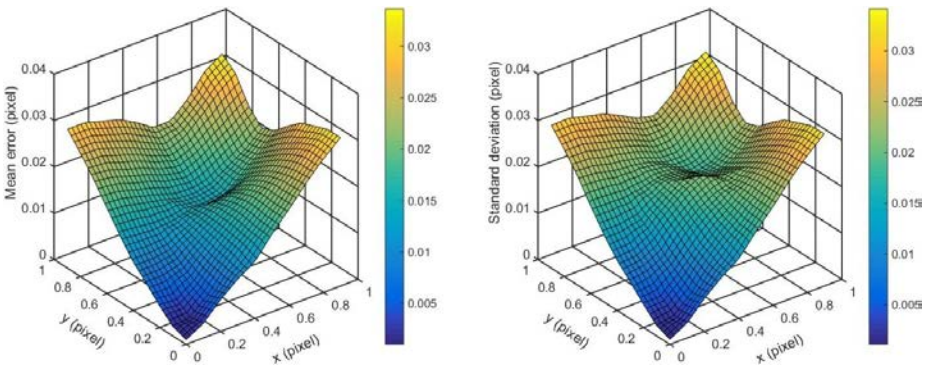


(c)



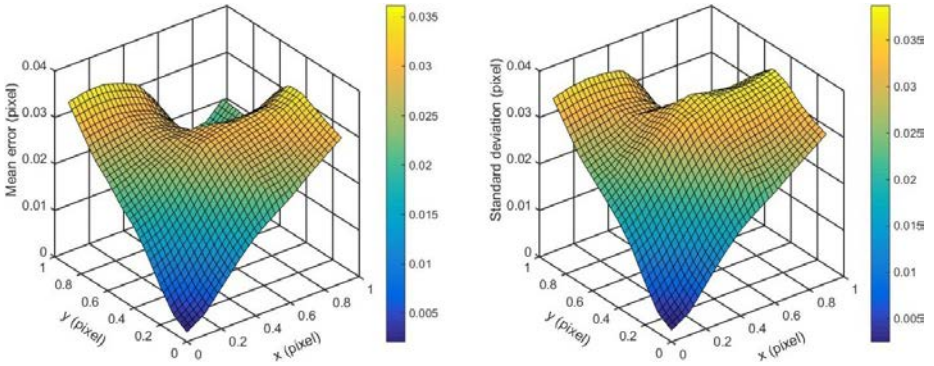
(d)

Fig. 8. (Continued)

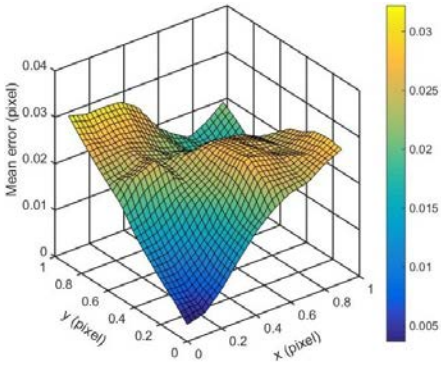
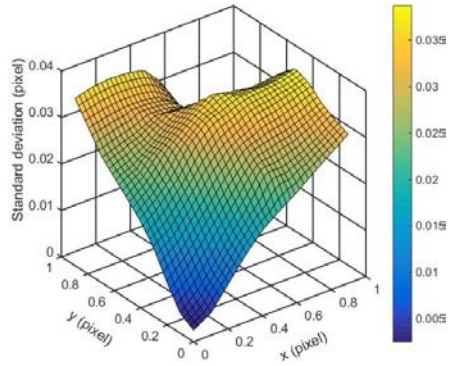


(a)

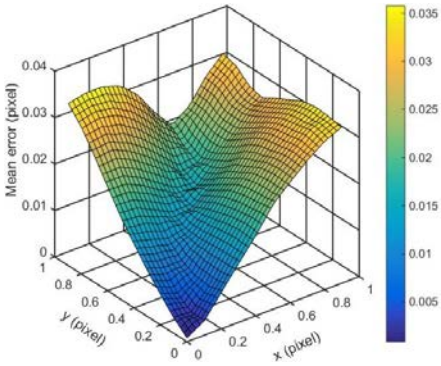
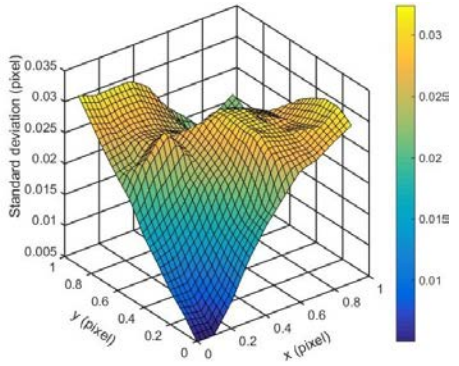
Fig. 9. Graphs of mean error field and square deviation field of the displacement of solar magnetic field images in EUV wavelengths by nonlinear gradient iterative algorithm, and 30% increase in brightness: (a) in wavelength 94 Å, (b) in wavelength 131 Å, (c) in wavelength 211 Å and (d) in wavelength 335 Å.



(b)



(c)



(d)

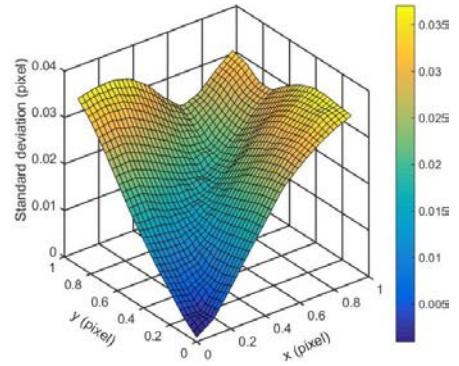


Fig. 9. (Continued)

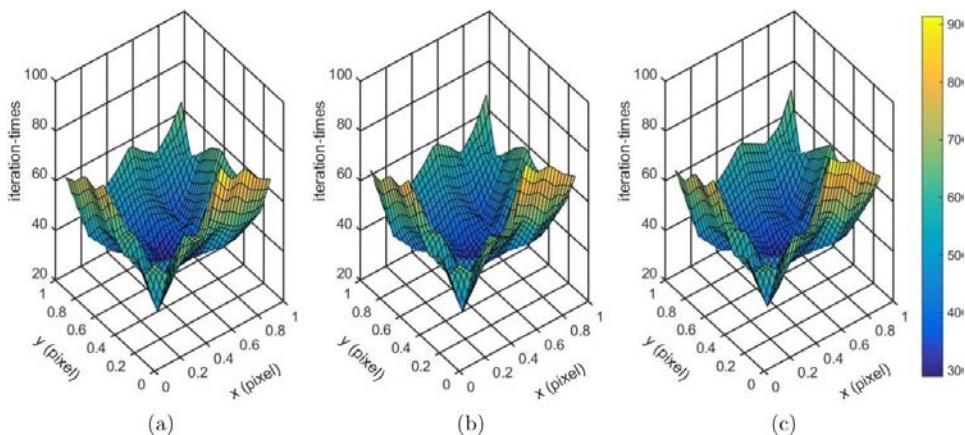


Fig. 10. Comparison of iteration times of deformed displacement field images measurement in EUV wavelengths by nonlinear gradient iterative algorithm in 94 Å wavelength: (a) 10% increase in brightness, (b) 20% increase in brightness and (c) 30% increase in brightness.

from 0.1 to 0.9 pixels by a pace of 0.1 pixels in x direction and y direction in three intensity change models is given in Figs. 10–13. The figures of iterations shown in Figs. 10 and 13 are quite similar due to their semblable histogram distribution, and the iterations around the sub-pixel displacement are much more than those in the center. Meanwhile, the figures of iterations shown in Figs. 11 and 12 are also quite similar owing to their similar histogram distribution, and the iterations of sub-pixel displacement in the four corners of x direction and y direction are less, and the iterations of sub-pixel displacement in the four peaks of the center are much more.

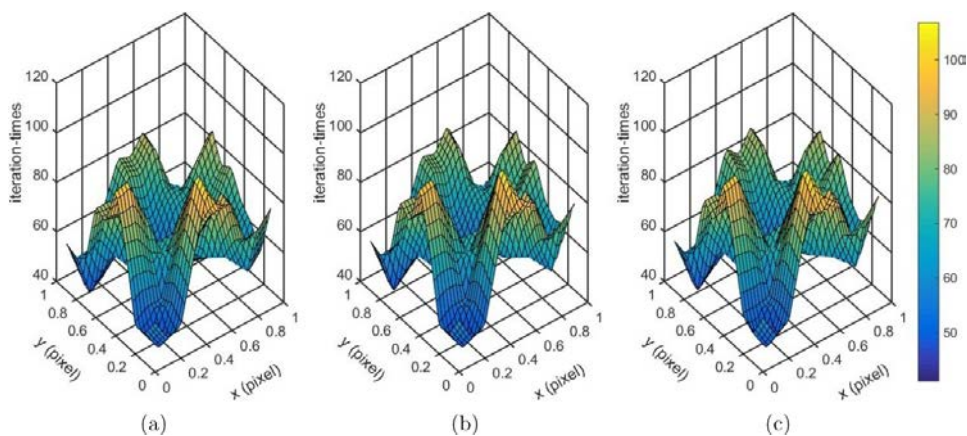


Fig. 11. Comparison of iteration times of deformed displacement field images measurement in EUV wavelengths by nonlinear gradient iterative algorithm in 131 Å wavelength: (a) 10% increase in brightness, (b) 20% increase in brightness and (c) 30% increase in brightness.

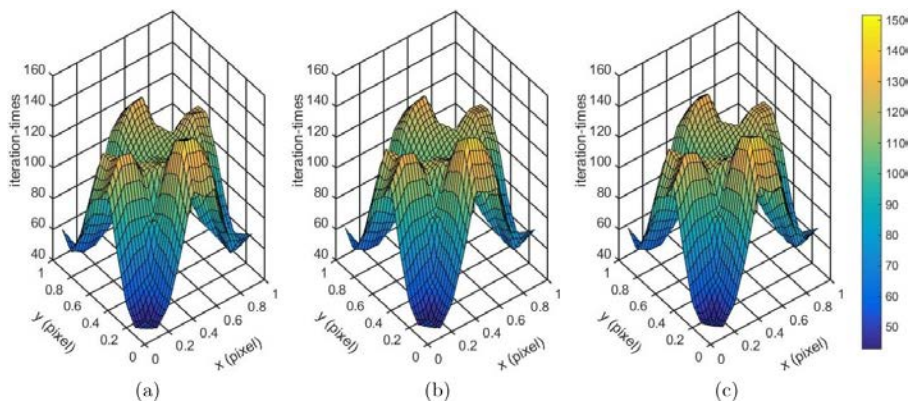


Fig. 12. Comparison of iteration times of deformed displacement field images measurement in EUV wavelengths by nonlinear gradient iterative algorithm in 211 Å wavelength: (a) 10% increase in brightness, (b) 20% increase in brightness and (c) 30% increase in brightness.

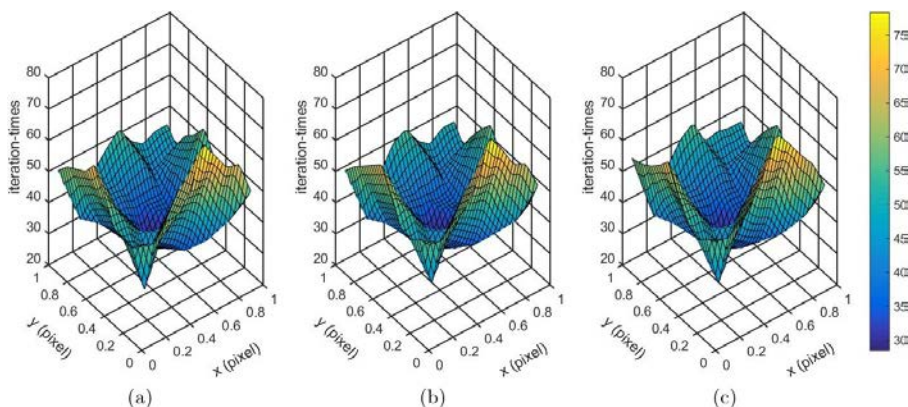


Fig. 13. Comparison of integration times of deformed displacement field images measurement in EUV wavelengths by nonlinear gradient iterative algorithm in 335 Å wavelength: (a) 10% increase in brightness, (b) 20% increase in brightness and (c) 30% increase in brightness.

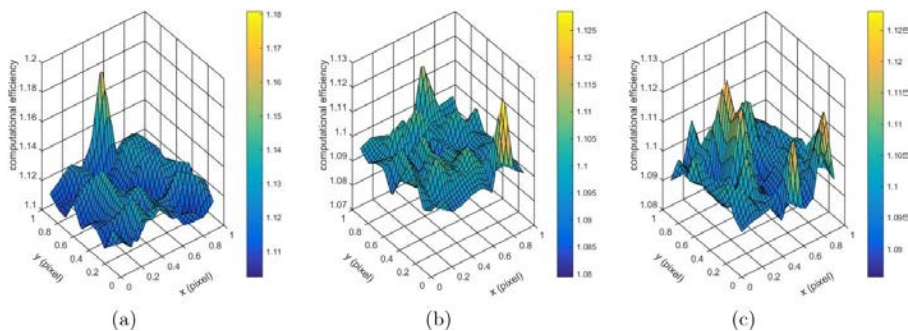


Fig. 14. Comparison of computational time of deformed displacement field images measurement in EUV wavelengths by parabolic least-square fit algorithm in 94 Å wavelength: (a) 10% increase in brightness, (b) 20% increase in brightness and (c) 30% increase in brightness.

Y. Liu et al.

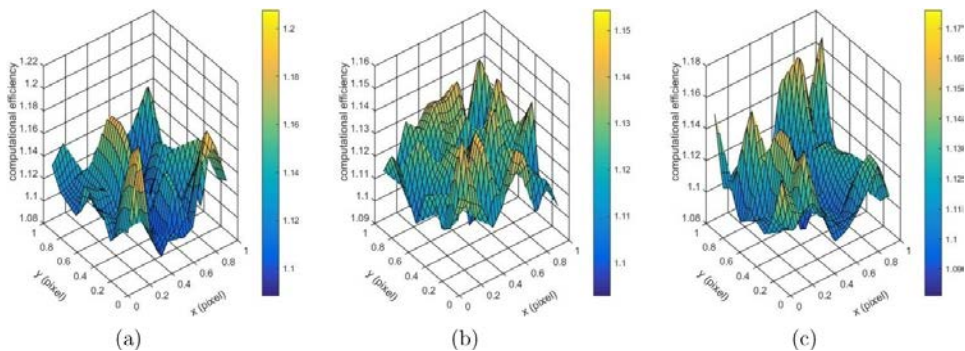


Fig. 15. Comparison of computational time of deformed displacement field images measurement in EUV wavelengths by parabolic least-square fit algorithm in 131 Å wavelength: (a) 10% increase in brightness, (b) 20% increase in brightness and (c) 30% increase in brightness.

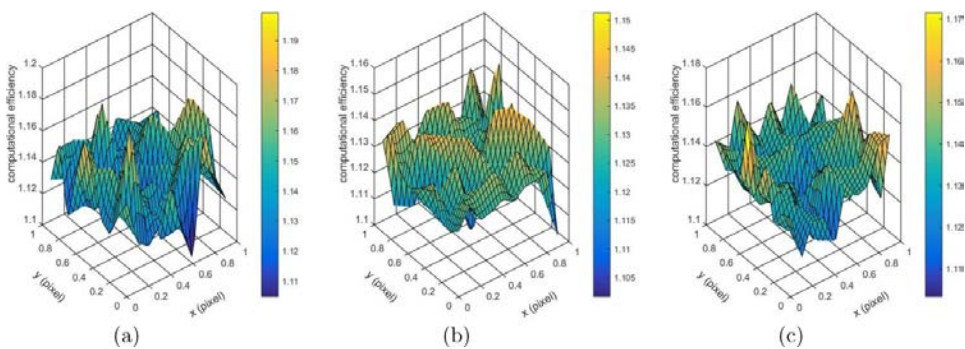


Fig. 16. Comparison of computational time of deformed displacement field images measurement in EUV wavelengths by parabolic least-square fit algorithm in 221 Å wavelength: (a) 10% increase in brightness, (b) 20% increase in brightness and (c) 30% increase in brightness.

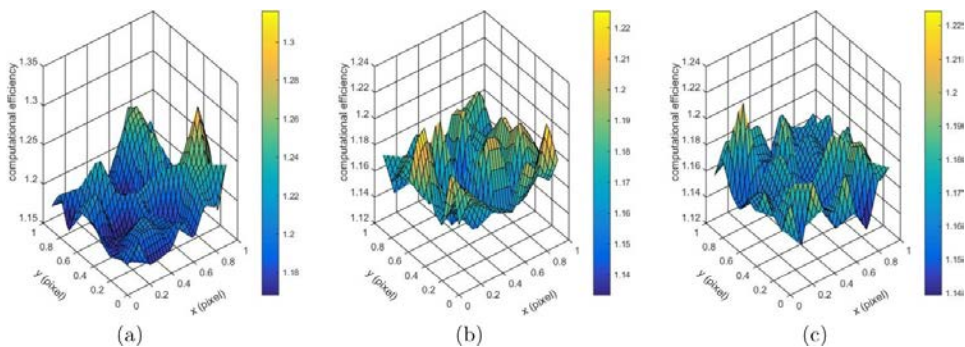


Fig. 17. Comparison of computational time of deformed displacement field images measurement in EUV wavelengths by parabolic least-square fit algorithm in 335 Å wavelength: (a) 10% increase in brightness, (b) 20% increase in brightness and (c) 30% increase in brightness.

It is obvious that the algorithm in this paper is insensitive to the solar magnetic evolution, and has better accuracy.

A comparison of computational time of deformed displacement field images measurement in EUV wavelengths by parabolic least-square fit algorithm as ranged from 0.1 to 0.9 pixels by a pace of 0.1 pixels in x direction and y direction in three intensity change models is given in Figs. 14–17.

4. Conclusion

In this paper, a more robust deformed displacement analysis algorithm of solar magnetic field images in EUV wavelengths based on nonlinear gradient interaction and crossing method is presented. Both the cubic and linear factors of the solar magnetic field evolution are taken into account, and also satellite attitude changes during solar magnetic field images acquisition and the various sub-pixel displacement measurement functions, which models can be easily incorporated into. So as to study and evaluate the capability of the algorithm, lots of simulated experiments are done. These experiments results have shown that, using this method, the square deviation and mean error are all less than 5% in all EUV wavelengths, and similar behavior has been shown in different intensity variation cases which suggest that the method in this paper has well accuracy and stability for the solar magnetic evolution. This algorithm is mainly applied in two aspects, on the one hand, the continuous solar EUV images collected by the space solar imager are accurately matched on the ground to enhance the signal-to-noise ratio of the images, so that the image resolution is higher. This application does not require high real-time computing, and this algorithm is very suitable. On the other hand, the sun image displacement caused by the satellite itself and solar evolution is detected in real time by the solar images on space solar telescope, but this application of the algorithm requires some preconditions. High speed hardware calculation unit is required to ensure fast calculation of iteration process, and the algorithm needs to be simplified according to practical application, and the darker EUV signal is enhanced to allow rapid imaging by image intensifier. The intensifier MCP and the photomultiplier are required, enhancing a single photon to thousands of photons, which is illuminated to the detector, and the darker EUV signal is enhanced to make it rapidly image. Moreover, the potential of real-time displacement measurement in space solar telescope should be studied in future work. Meanwhile, the further research extending this method to be used in X wavelength still has much work to be done. And continuous phase removal algorithm in exposure time will be my next work.

Acknowledgments

This work is supported by the Strategic Priority Research Program of Chinese Academy of Science (CAS). Grant No. XDA15320103.

Author Contributions

All of the authors have made a contribution to this work, either in the model processing or in the measurement verification. Y. L., K.-F. S. and B. C. managed this work; Y. L., Z.-W. H. performed the experiments; Y. L., K.-F. S. and X.-D. W. analyzed the data; Y. L. and J.-L. M. wrote the paper.

References

1. J. A. Caballer, J. E. P. Pascua and L. A. Ruiz, Evaluating fourier cross-correlation sub-pixel registration in landsat images, *Remote Sens.* **9** (2017) 1051.
2. P. Hajireza, W. Shi, K. Bell, R. J. Paproski and R. J. Zemp, Non-interferometric photo acoustic remote sensing microscopy, *Light: Science & Applications* **6** (2017) 16278.
3. K. L. Hu, Y. Y. Deng and Q. Song, Analysis about the precision of correlation tracker in space solar telescope (SST), in *Proc. SPIE 4853, Innovative Telescopes and Instrumentation for Solar Astrophysics, Astronomical Telescopes and Instrumentation*, United States, eds. S. L. Keil, S. V. Avakyan (22–28 August 2002, Waikoloa, Hawai'i).
4. T. Hua, H. M. Xie, S. Wang, Z. X. Hu, P. W. Chen and Q. M. Zhang, Evaluation of the quality of a speckle pattern in the digital image correlation method by mean subset-fluctuation, *Optics & Laser Technology* **43** (2011) 9–13.
5. W. Huang, C. F. Ma and Y. H. Chen, Displacement measurement with nano scale resolution using a coded micro-mark and digital image correlation, *Opt. Eng.* **53** (2014) 124103.
6. D. Inamdar, G. Leblanc, R. J. Soffer and M. Kalacska, The correlation coefficient as a simple tool for the localization of errors in spectroscopic imaging data, *Remote Sens.* **10** (2018) 231.
7. S. Jiang, X. B. Zhang, Y. Zhang, C. R. Hu and R. Zhang, Subnanometer-resolved chemical imaging via multivariate analysis of tip-enhanced Raman maps, *Light: Science & Applications* **6** (2017) 17098.
8. T. K. Kim, N. V. Pogorelov and G. P. Zank, Modeling the solar wind at the Ulysses, Voyager, and New Horizons spacecraft, *Physics — Space Physics* **832** (2016) 1–9.
9. F. Ling, G. M. Foody, X. Li, Y. Zhang and Y. Du, Assessing a temporal change strategy for sub-pixel land cover change mapping from multi-scale remote sensing imagery, *Remote Sens.* **8** (2016) 642.
10. X. Y. Liu, Q. C. Tan and L. Xiong, Performance of iterative gradient-based algorithms with different intensity change models in digital image correlation, *Opt. Laser Technol.* **44** (2012) 1060–1067.
11. L. B. Meng, G. C. Jin and X. F. Yao, Application of iteration and finite element smoothing technique for displacement and strain measurement of digital speckle correlation, *Opt. Lasers Eng.* **45** (2007) 57–63.
12. B. Pan and H. M. Xie, Digital image correlation using iterative least squares and pointwise leastsquares for displacement field and strain field measurements, *Opt. Lasers Eng.* **47** (2009) 865–874.
13. B. Pan, H. M. Xie, B. Q. Xu and F. L. Dai, Performance of sub-pixel registration algorithms in digital image correlation, *Measurement Science and Technology* **17** (2006) 1615–1621.
14. S. Toshifumi and E. Chris, Image stabilization system on SOLAR-B solar optical telescope, in *Proc. SPIE 5487, Optical, Infrared, and Millimeter Space Telescopes SPIE Astronomical Telescopes + Instrumentation*, ed. C. M. John (21–25 June 2004, Glasgow, United Kingdom).

15. R. Volkmer, J. Bosch and B. Feger, Image stabilisation system of the photospheric and helioseismic imager, in *Space Telescopes and Instrumentation 2012: Optical, Infrared, and Millimeter Wave, SPIE Astronomical Telescopes + Instrumentation* eds. M. C. Clampin, G. G. Fazio and H. A. MacEwen (1–6 July 2012, Amsterdam, The Netherlands).
16. V. P. Lukin, L. V. Antoshkin, N. N. Botygina, Modified correlation tracker algorithm for tip-tilt correction system and project ANGARA on the Big Solar Vacuum Telescope, in *Proc. SPIE 6272, Advances in Adaptive Optics II, SPIE Astronomical Telescopes + Instrumentation* ed. B. L. Ellerbroek (24–31 May 2006, Orlando, Florida, United States).
17. K. Wu, Q. Du, Y. Wang and Y. Yang, Supervised sub-pixel mapping for change detection from remotely sensed images with different resolutions, *Remote Sens.* **9** (2017) 284.
18. Y. Xu, L. Lin and D. Y. Meng, Learning-based sub-pixel change detection using coarse resolution satellite imagery, *Remote Sens.* **9** (2017) 709.
19. O. I. Yakovlev, Determination of the solar-wind velocity, density, power, and acceleration by the method of radio sounding of the near-solar plasma by the spacecraft signals, *Radiophys. Quantum Electron.* **57** (2014) 313–325.
20. Z. F. Zhang, Y. L. Kang, H. W. Wang, Q. H. Qin, Y. Qiu and X. Q. Li, A novel coarse-finesearch scheme for digital image correlation method, *Measurement* **39** (2006) 710–718.



Yang Liu is currently an Assistant Researcher at Changchun Institute of Optics, Fine Mechanics and Physics, Chinese Academy of Sciences, Changchun, China. He obtained his B.S. degree in Electronic Information Science and Technology from Jilin University,

Changchun, Jilin, China in 2009, his M.S. degree in Circuit and System from Jilin University in 2012. He is now studying for a doctor's degree from University of Chinese Academy of Sciences, Beijing 100049, China. He authorized a number of Chinese invention patents and applied for an American patent. His scientific interests include researching on image processing of space solar imager.



Kefei Song is currently a Professor at Changchun Institute of Optics, Fine Mechanics and Physics, Chinese Academy of Sciences, Changchun, China. She obtained her B.S. degree from Changchun University of Technology, Changchun, Jilin, China in 1988, her M.S. degree

from Changchun Institute of Optics, Fine Mechanics and Physics, Chinese Academy of Sciences. She authorized a number of Chinese invention patents. She has published many technical papers. Her scientific interests include application of space remote sensing measurement and control technology and embedded system.



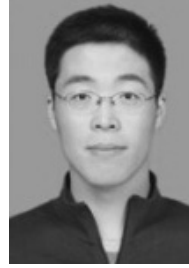
Xiaodong Wang is currently a Professor at Changchun Institute of Optics, Fine Mechanics and Physics, Chinese Academy of Sciences, Changchun, China. He obtained his Ph.D. degree from Changchun Institute of Optics, Fine Mechanics and Physics, Chinese

Academy of Sciences in 2002. He has published more than 30 technical papers and authorized a number of Chinese invention patents. His scientific interests include imaging technology and information processing of space optical remote sensing instrument.



Bo Chen is currently a Professor at Changchun Institute of Optics, Fine Mechanics and Physics, Chinese Academy of Sciences, Changchun, China. He obtained his B.S. degree Department of Physics from Jilin University, Changchun, Jilin, China in 1984. He has

published many technical papers and authorized a number of Chinese invention patents. His scientific interests include soft X-ray — extreme ultraviolet — band optical and spatial optical studies.



Junlin Ma is currently an Assistant Researcher at Changchun Institute of Optics, Fine Mechanics and Physics, Chinese Academy of Sciences, Changchun, China. He obtained his B.S. degree in mechanical engineering and automation from Harbin Institute of Technology in 2009, his M.S. degree in mechatronic engineering from Harbin Institute of Technology in 2011. He has authorized a number of Chinese invention patents. His scientific interests include optomechanical design and structural optimization.



Zhenwei Han is currently a Research Associate at Changchun Institute of Optics, Fine Mechanics and Physics, Chinese Academy of Sciences, Changchun, China. He obtained his B. S. degree from Dalian University of Technology in 2007, his M.S. degree from Tianjin University in 2009. He is now studying for a doctor's degree from University of Chinese Academy of Sciences, Beijing 100049, China. His scientific interests include spatial short-wavelength imager signal processing.